Supplementary Information

Machine-learning-empowered FDTD/FEM simulations for predictive solar energy absorption in plasmonic metamaterial nanocavity arrays

Zahra Ashrafi-Peyman,[a] Amir Dashti,[b] Amir Jafargholi,[c] John L. Zhou,*[b] and Alireza Z. Moshfegh*[a,d]

a. *Department of Physics, Sharif University of Technology, Tehran 11555-9161, Iran.*
b. *Centre for Green Technology, School of Civil and Environmental Engineering, University of Technology Sydney, Sydney, NSW 2007, Australia.*
c. *Laboratory of Wave Engineering, School of Electrical Engineering, Swiss Federal Institute of Technology in Lausanne (EPFL), Lausanne, Switzerland.*
d. *Center for Nanoscience and Nanotechnology, Institute for Convergence Science & Technology (ICST), Sharif University of Technology, Tehran 11365-8639, Iran.*

**Corresponding authors: moshfegh@sharif.edu & junliang.zhou@uts.edu.au*

Contents

Abbreviations & Nomenclature:

A	Absorption
AARD	Average Absolute Relative Deviation
AM1.5	Air Mass Coefficient 1.5
ANFIS	Adaptive Neuro-Fuzzy Inference System
E-Field	Electric Field
FDTD	Finite-Difference Time Domain
FEM	Finite Element Method
GP	Genetic Programming
h	Height of the TiN Nanotube
LSPR	Localized Surface Plasmon Resonance
ML	Machine Learning
MSE	Mean Squared Error
MTM	Metamaterial
NIR	Near-Infrared
P	Period
PBIAS	Percent Bias
PSO	Particle Swarm Optimization
R	Major radius of the TiN Nanotube
r	Minor radius of the TiN Nanotube
R^2	Correlation Coefficient
RMSD	Root Mean Square Difference
SPPs	Surface Plasmon Polaritons
STD	Standard Deviation
STEG	Solar Thermoelectric Generator
STPV	Solar Thermophotovoltaic
t	Thickness of the TiO_2 Thin Layer
TE	Transverse Electric
TM	Transverse Magnetic
UV	Ultraviolet
Vis	Visible
λ	Wavelength
Z	Impedance
ε	Permittivity
ω	Angular Frequency

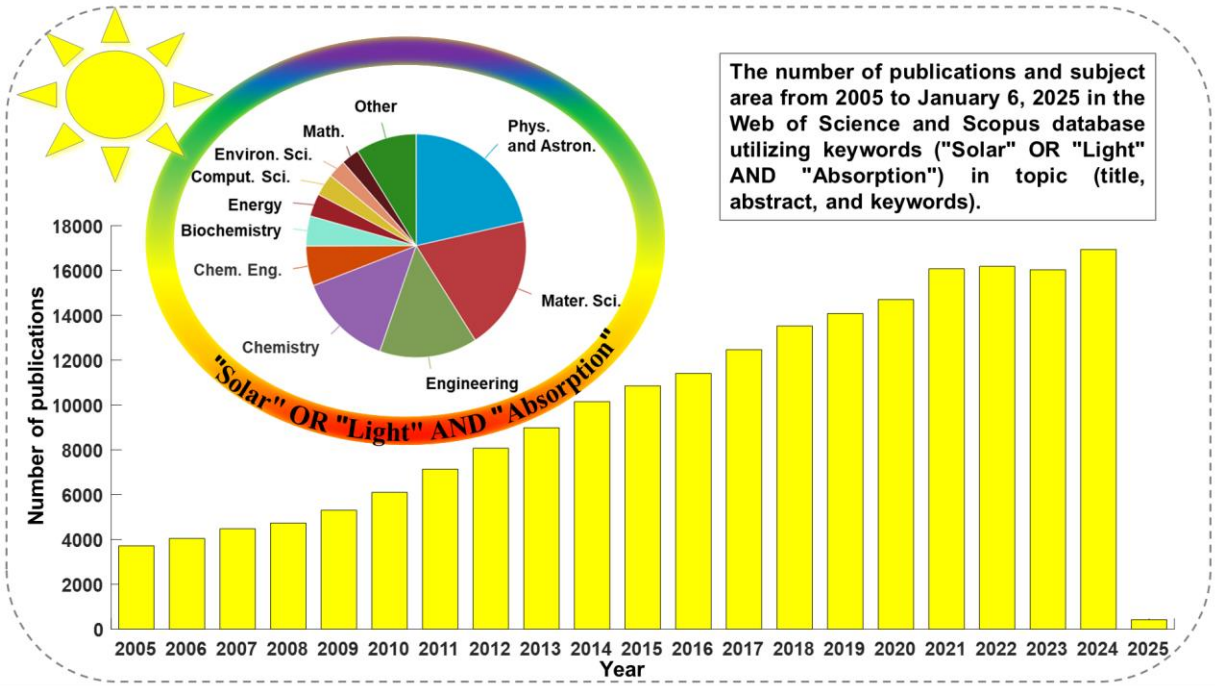

Fig. S1 The number of publications in the Web of Science citation database and documents by subject area in the Scopus database utilizing keywords ("Solar" OR "Light") AND ("Absorption") in topic (title, abstract, and keywords). Accessed on January 6, 2025.

Supplementary Note 1: Properties of TiN and TiO_2 materials.

Although gold (Au)[1,2] and silver (Ag)[3,4] are extensively studied for applications linked to hot electrons, their limited practical uses in solar energy stem from their high cost, low reserves, poor thermal and chemical stability, and narrow absorption peaks. Additionally, these disadvantages restrict their large-scale applications in hot electron generation, thermal photovoltaics, thermal emission, and solar absorbers. Then, TiN[5,6] is appropriate for harsh environments and high-temperature applications such as solar steam,[7] solar thermoelectric power,[8] and solar thermophotovoltaic[9] due to its exceptional thermal, chemical, and mechanical stability. Low electrical resistivity, high electron mobility, and metallic conductivity are some of its electrical characteristics.[10] Compared to Au, which has a typical value of 5.4 eV, TiN has a work function of 3.2–4.4 eV against vacuum.[1,11] It is a good option for hot carrier-enhanced solar energy conversion since its work function is larger than or equal to the electron affinity of the majority of semiconductor metal oxides utilized in photocatalysis, such as TiO_2. The whole solar spectrum is covered by TiN nanostructures because they exhibit strong plasmon resonances in the red.[12]

Concerning optical properties, compared to Au nanoparticles, TiN can inject twice as many hot electrons into TiO_2, resulting in broadband absorption efficiency spanning the 500–1200 nm wavelength range.[12] Together with TiO_2, it also forms an ohmic junction, which permits "downhill" hot electron collection and raises conversion efficiencies over the gold.[12] A summary of the operation ranges and advantageous of material properties for TiN, Ag, and Au is presented in Table S1 based on data adapted from References 1 and 13. Conversely, TiO_2, a widely used benchmark material in the environmental and energy sectors, is a successful semiconductor for

plasmonic nanostructures because of its unique electronic and photoelectrochemical properties, non-toxicity, cost-effectiveness, and photo/chemical stability.[14,15] It could be applied in solar cells, water splitting, and wastewater treatment.[16,17] However, due to its wide band gap (~3.2 eV),[14] it has a low absorption response and is insensitive to visible light. Nevertheless, when integrated with plasmonic materials such as TiN, TiO_2 can be activated in the visible range of the solar spectrum through plasmon-induced hot electron injection, enabling visible-light-driven functionalities.[12] Thus, in order to increase the photocatalytic efficiency of wide band gap semiconductors in visible light, great efforts have been made recently to design and realize plasmonic-coupled low-bandgap transition metal oxides (TiO_2).[14,18] Thus, this study presents an exciting path towards new solar energy harvesting devices with high absorption ability.

Table S1 Material properties and operation ranges for TiN, Ag, and Au based on data adapted from References 1 and 13.

	Epsilon Near Zero (ENZ) (nm)	Work Function (eV)	Heat Capacity ($MJm^{-3}K^{-1}$)	Melting point (°C)	Low loss	Thermal Stability	Tuneable Carrier Concentration	UV/Vis Absorption	NIR Absorption
TiN	**~495**	**3.2-4.4**	**3.2**	**~2950**	✗	✓	✓	✓	✓
Ag	**<300**	**4.3-4.6**	**2.5**	**~962**	✓	✗	✗	✓	✗
Au	**<300**	**5.4**	**2.5**	**~1064**	✓	✗	✗	✓	✗

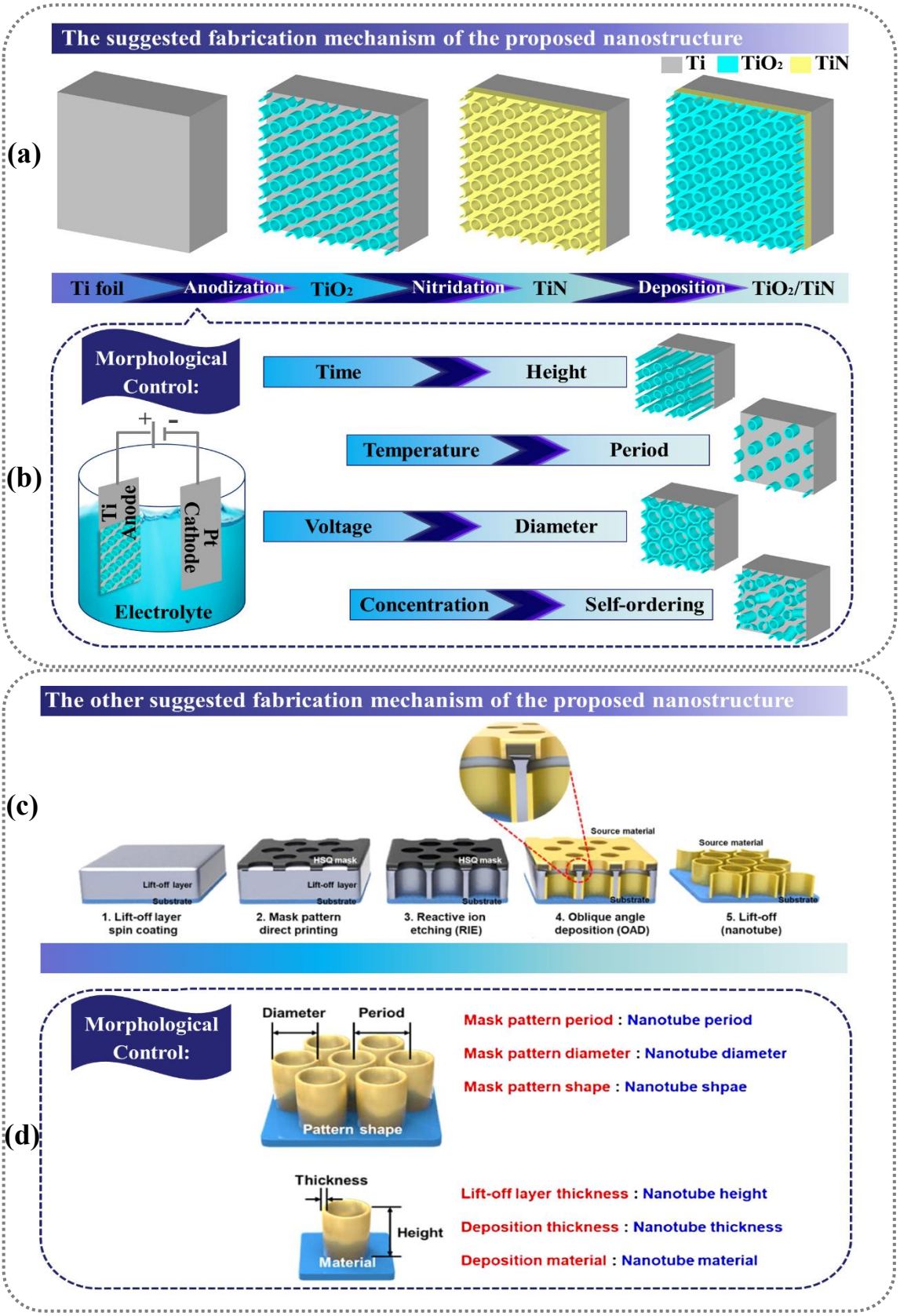

Fig. S2 (a) A schematic of the suggested process to fabricate the proposed nanostructure using

lithography-free technology. Suggested steps for the fabrication of designed nanostructures. (b) The effect of different parameters in the anodization process on the geometry of the proposed nanostructure. (c) A schematic of the other suggested process to fabricate the proposed TiN nanotube array using direct printing (soft lithography) technology. Suggested steps for the fabrication of TiN nanotubes. Since direct printing can quickly and accurately generate nano- and micro-scale patterns over a large area, it could be used in this process to fabricate the deposition hydrogen silsesquioxane (HSQ) mask. After that, oblique angle deposition (OAD) could be used to deposit nanotubes. This method produces different nanostructures due to the shadowing effect when the substrate and source material are tilted with respect to each other. Conventional nanotube production methods are limited by material constraints; however, these limitations have been addressed by the application of e-beam evaporation for deposition. (d) Morphological control of the TiN nanotube as a function of several fabrication parameters. (c, d) Reprinted with permission from Reference (19). Copyright 2024 Elsevier.

Supporting Note 2: Influence of different structural parameters.

To determine the optimal geometry for maximizing absorption, we performed a detailed parametric sweep of key structural parameters, as presented in Fig. S3. In Fig. S3a, the sweep period (*P*) is reduced from 300 nm to 180 nm, resulting in a decrease in the gap between the nanotubes and an increase in the absorption width. This is actually a nanoantenna property of

nanotubes. In contrast, until *P* reaches its optimum (*P*=240 nm), the rate of absorption ability rises with decreasing *P*. Following that, however, the amount of absorption also falls with decreasing *P*, particularly in the regions beyond λ=600 nm. Parameter *h* is varied in Fig. S3b from 100 nm to 225 nm, and as *h* increases, the absorption expands. However, as *h* increases, the absorption ability rises until it reaches its optimum (*h*=175 nm) and subsequently falls as *h* increases. Parameter *r* in Fig. S3c is swept between 30 and 70 nm. Up until it reaches the optimum parameter (*r*=60 nm), the absorption rate rises with an increase in *r*. After that, it falls as *r* increases. A sweep of parameter *R* from 70 nm to 110 nm is also shown in Fig. S3d. When *R* increases, the absorption ability rises until it reaches the optimal parameter (*R*=80 nm), after which it broadens but becomes less strong. As parameter *t* is increased and swept from 2.5 nm to 40 nm, Fig. S3e,f shows broad absorption with red shifts. Consequently, we can achieve tuneable absorption or broadband absorption with different wavelengths when *t* is changed. It is clear from Fig.s S3e,f that a range of parameter *t* variations ($2.5 < t < 20$ nm) has the least impact on the proposed absorber's absorption spectra capabilities and nearly maintains an absorption ability above 90%. This observation implies that there is a significant degree of manufacturing tolerance in the absorber, which makes the practical production procedure for this absorber simpler. The absorption ability, however, falls when the parameter *t* exceeds 20 nm. Depending on the absorption range of the intended applications, these graphs of changing parameters for optimization can be a useful data sheet for tuning optical absorption.

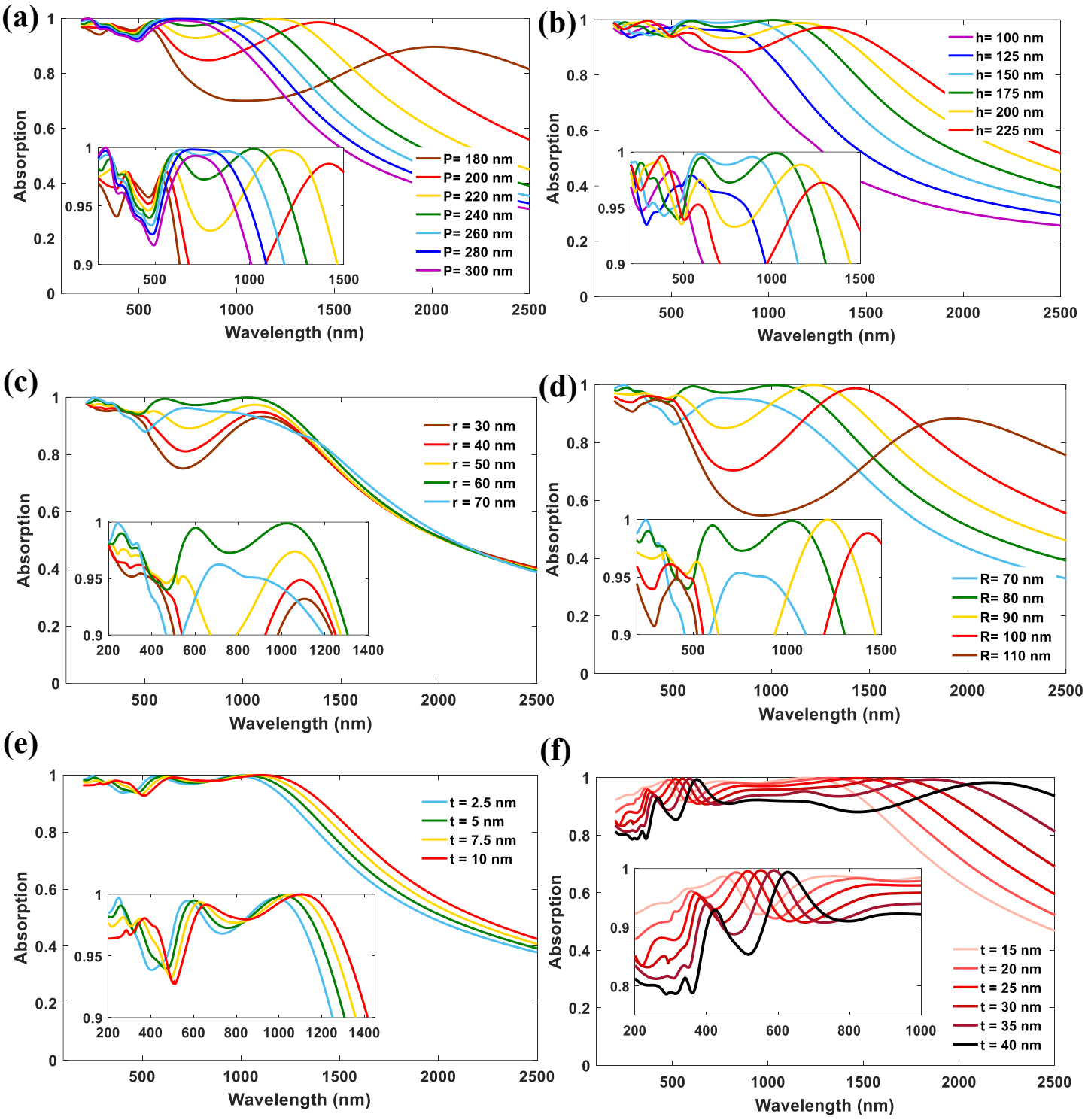

Fig. S3 Absorption spectra of the proposed absorber for Scale=1 (*P*=240 nm) with different geometric parameters. (a) period of a unit cell, *P*; (b) the height of the TiN nanotube, *h*; (c) the major radius, *R*; (d) the minor radius of the TiN nanotube, *r*; and (e, f) the thicknesses of the thin layer of TiO_2, *t*. The insets show its magnified section.

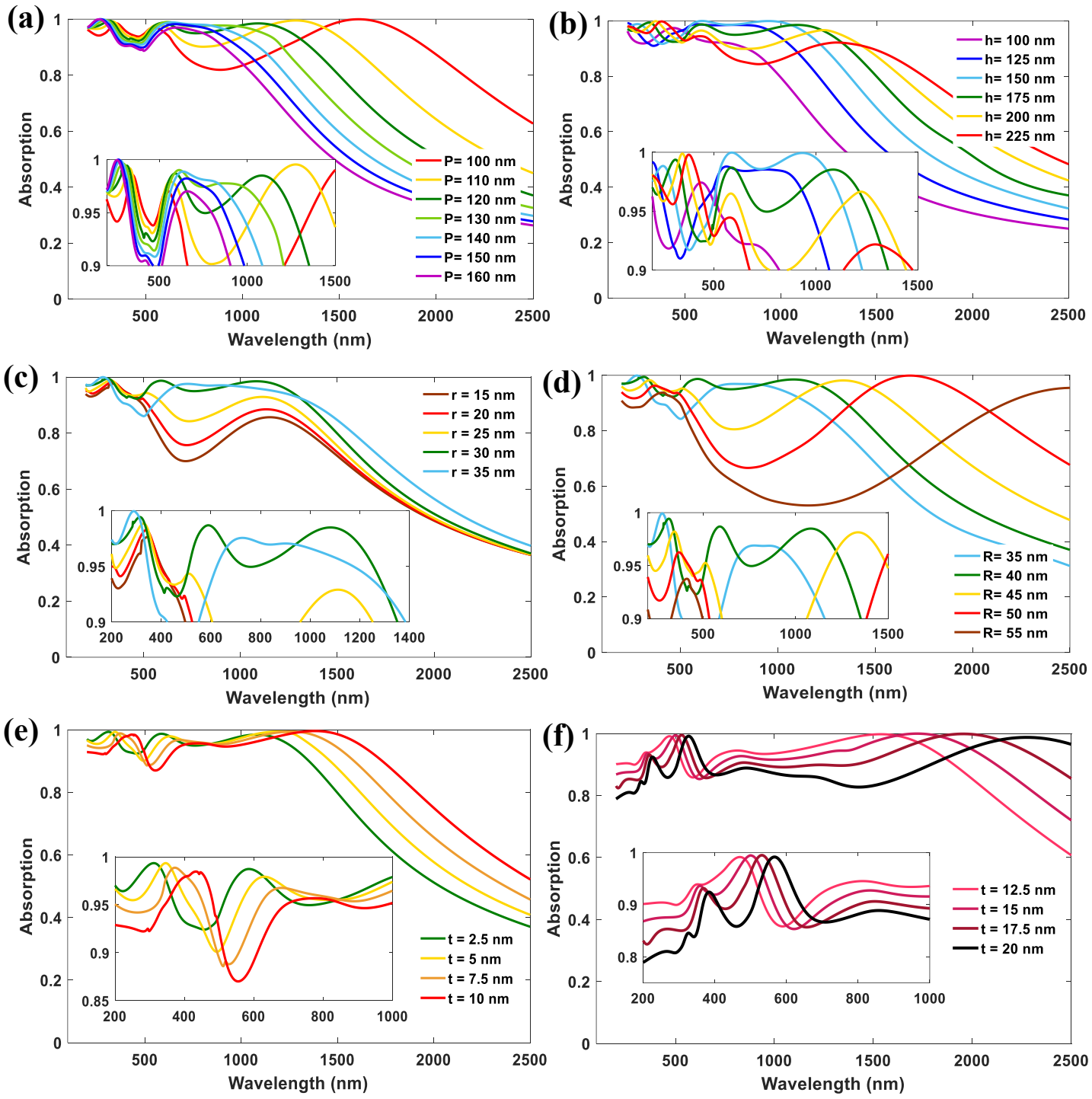

Fig. S4 Absorption spectra of the proposed absorber for Scale=1/2 (*P*=120 nm) with different geometric parameters. (a) period of a unit cell, *P*; (b) the height of the TiN nanotube, *h*; (c) the major radius, *R*; (d) the minor radius of the TiN nanotube, *r*; and (e, f) the thicknesses of the thin layer of TiO_2, *t*. The insets show its magnified section.

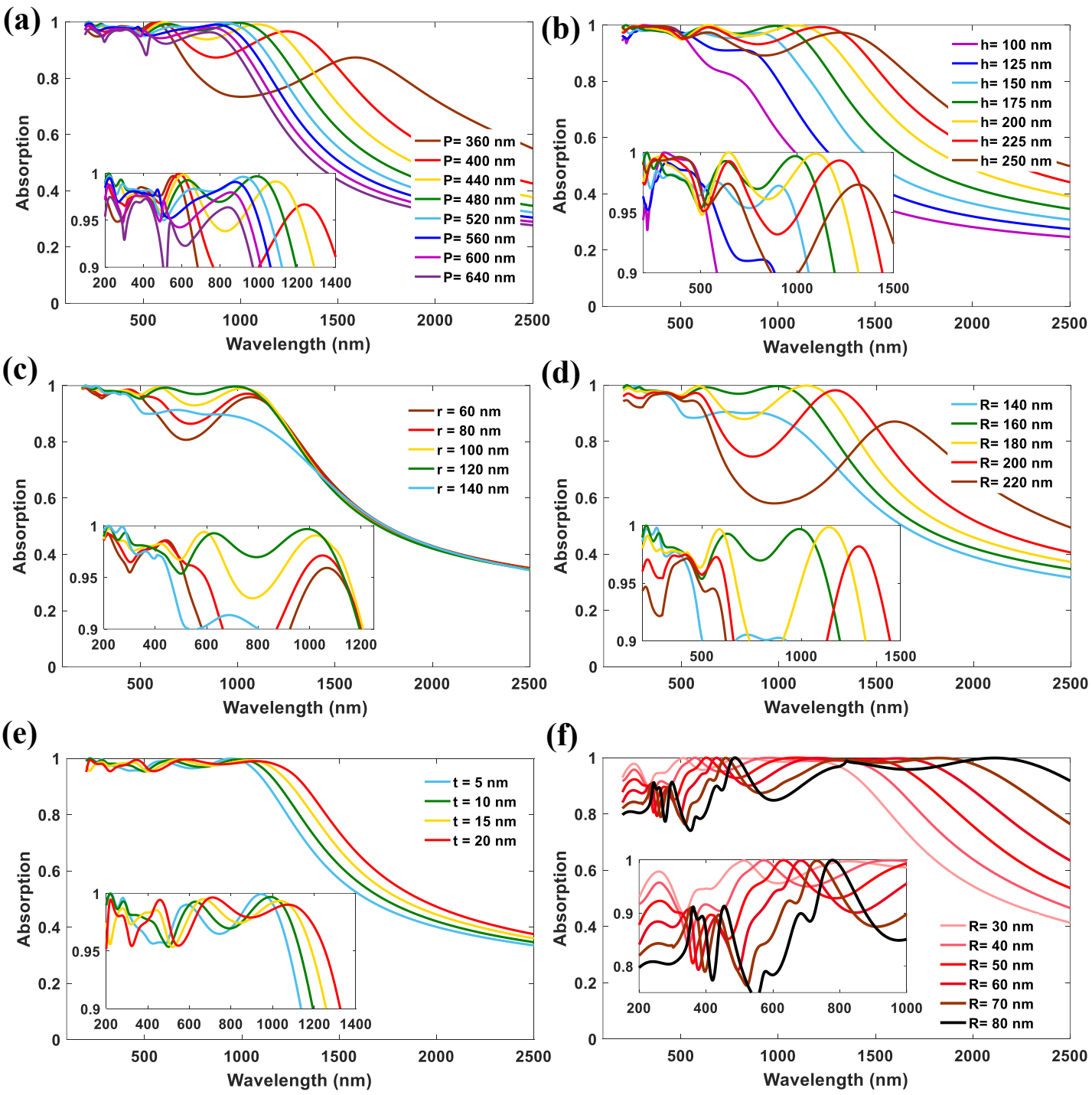

Fig. S5 Absorption spectra of the proposed absorber for Scale=2 (*P*=480 nm) with different geometric parameters. (a) period of a unit cell, *P*; (b) the height of the TiN nanotube, *h*; (c) the major radius, *R*; (d) the minor radius of the TiN nanotube, *r*; and (e, f) the thicknesses of the thin layer of TiO_2, *t*. The insets show its magnified section.

Table S2 The dimensions of the optimal geometric parameters of the proposed nanostructure with different scales along the x and y axes; all dimensions are in nm.

	P	***R***	***r***	***t***
Scale = 1/3	80	26.6	20	1.6
Scale = 1/2	120	40	30	2.5
Scale = 1	240	80	60	5
Scale = 2	480	160	120	10
Scale = 3	720	240	180	15

Supplementary Note 3: Influence of different configurations.

Fig. S6a depicts several nanotubes with square unit cells, and Fig. S6b displays the absorption spectra for each of these configurations. As seen in Fig. S6a, S1 stands for TiN nanotubes, S2 for TiO_2 nanotubes, S3 for S2 coated with a thin layer of TiN, and S4 for S1 coated with a thin layer of TiO_2. The TiN film substrate is positioned beneath the nanotubes in each of these instances. The square unit cell and the centered rectangular (CR) case exhibit absorption that is nearly identical to each other and repeats the same pattern, according to the absorption spectrum analysis shown in Fig. S6b and Fig. 3d. Additionally, Fig. S6c displays several nanopillar designs with CR unit cells, and Fig. S6 (d) exhibits the absorption spectra of each of these setups. As shown in Fig. S6c, P1 is a TiN nanopillar, P2 is a TiO_2 nanopillar, P3 is P2 coated with a thin layer of TiN, and P4 is P1 coated with a thin layer of TiO_2. According to the results in Fig. S6d, absorption in all nanopillar instances is acceptable in the 200–500 nm range but unfavorable in other regions.

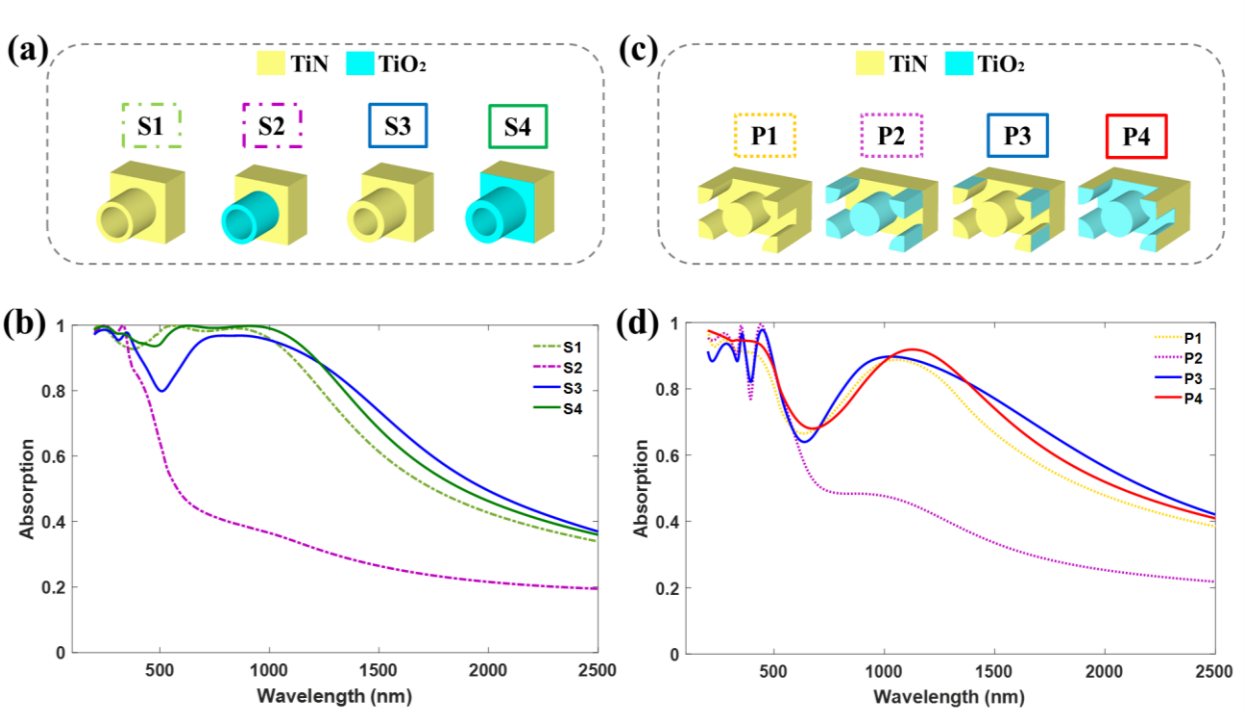

Fig. S6 (a) Different nanotubes in a square unit cell, and (b) the absorption diagram related to each of these cases. (c) Different nanopillars with CR unit cells, and (d) the absorption diagram related to each of these setups.

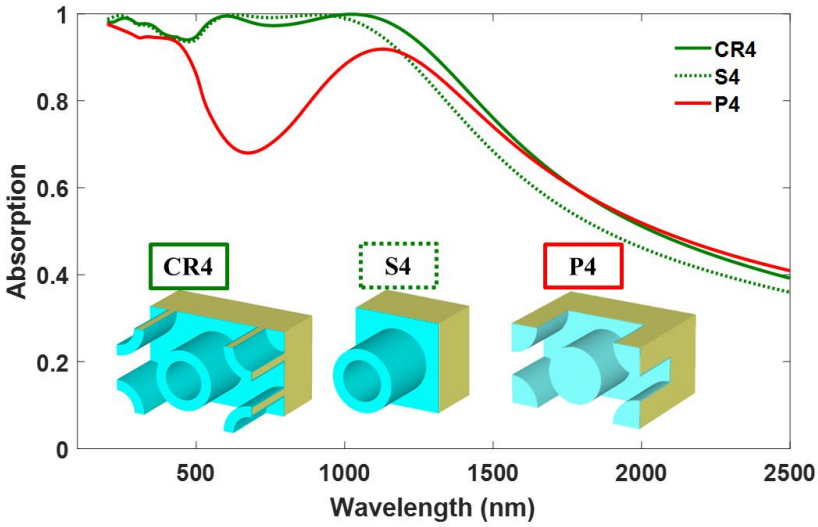

Fig. S7 Comparison of absorption spectra of nanopillars (P4) and nanotubes in square (S4) and centered rectangular (CR4) unit cells.

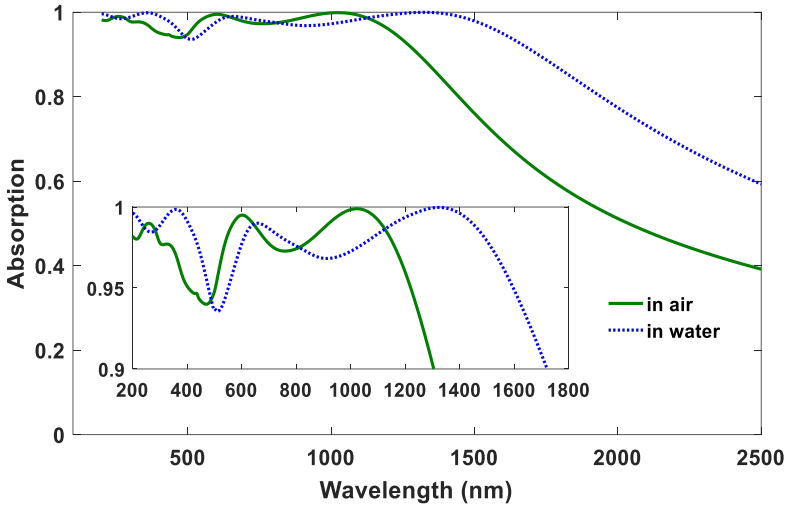

Fig. S8 Absorption spectra of the proposed nanostructure in air and water environments. The inset shows its magnified section.

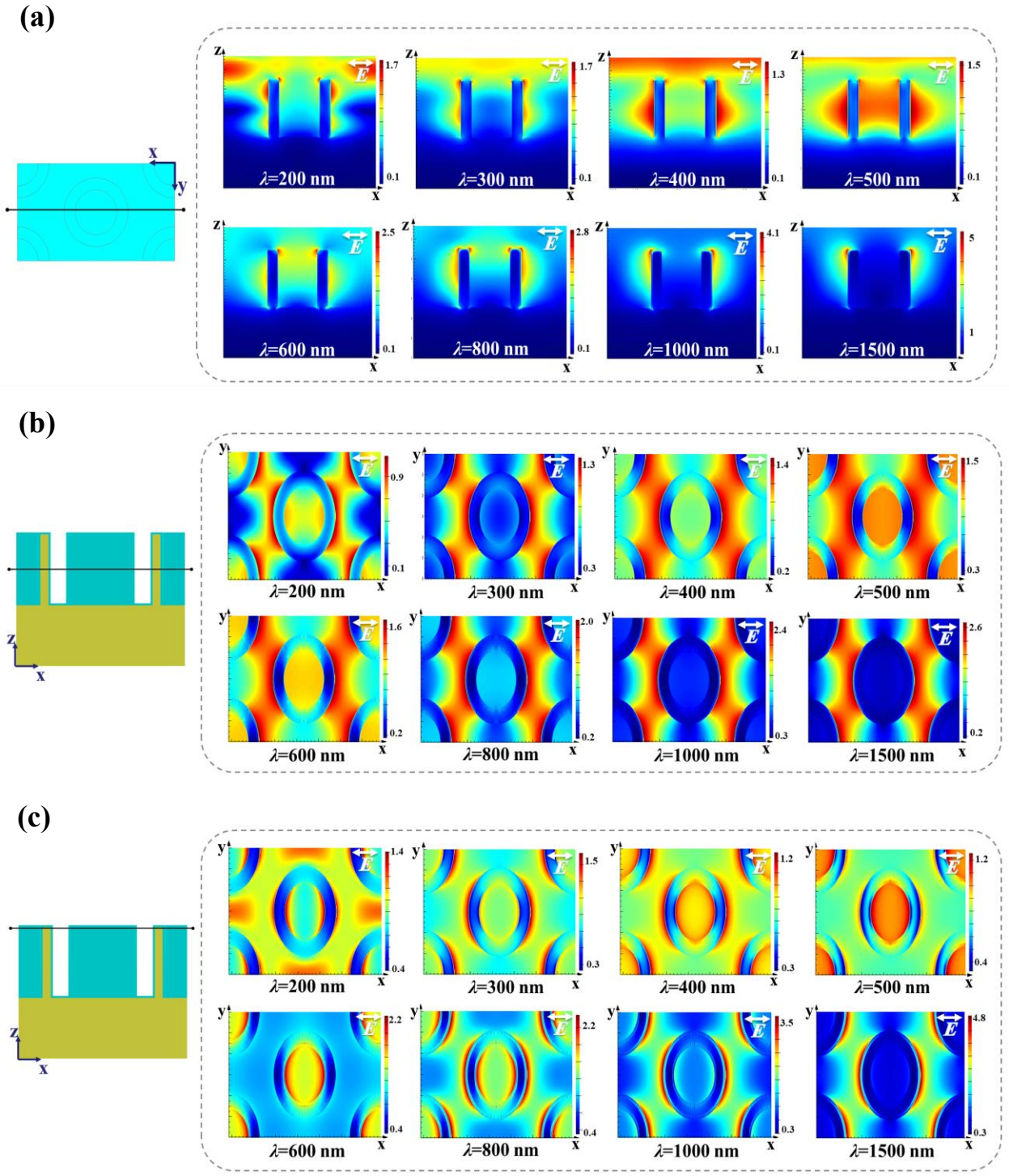

Continued on the next page

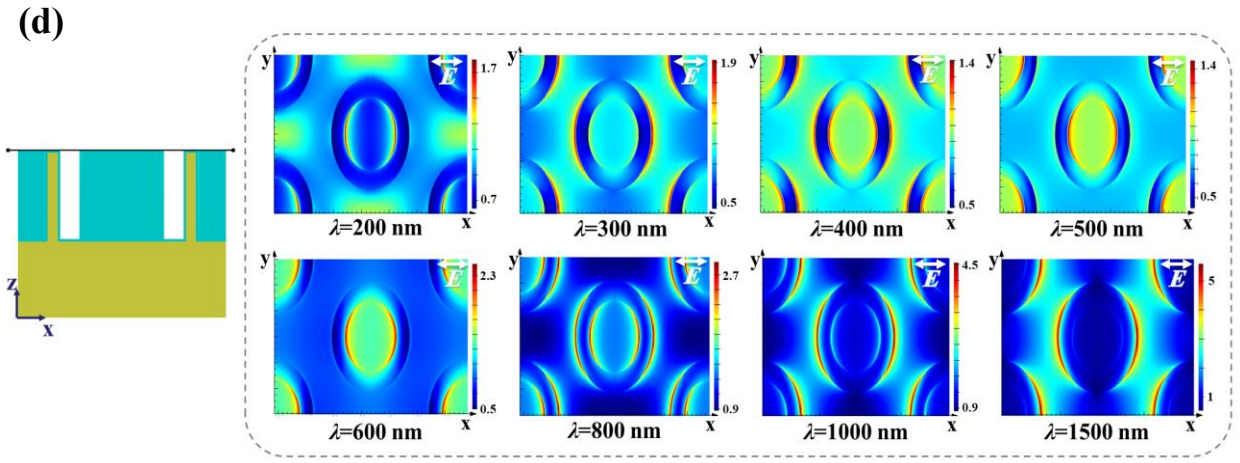

Fig. S9 Distribution of the E-field ($|E|/|E_o|$) under TM-polarized excitation at different wavelengths. (a) In the x-z plane, centered on the proposed MTM. In the x-y plane (b) at the middle of the height of nanotubes, (c) above the height of the TiN nanotubes, and (d) above the MTM. The schematics on the left illustrate the placement of the electric field monitor, which is oriented perpendicular to each displayed plane.

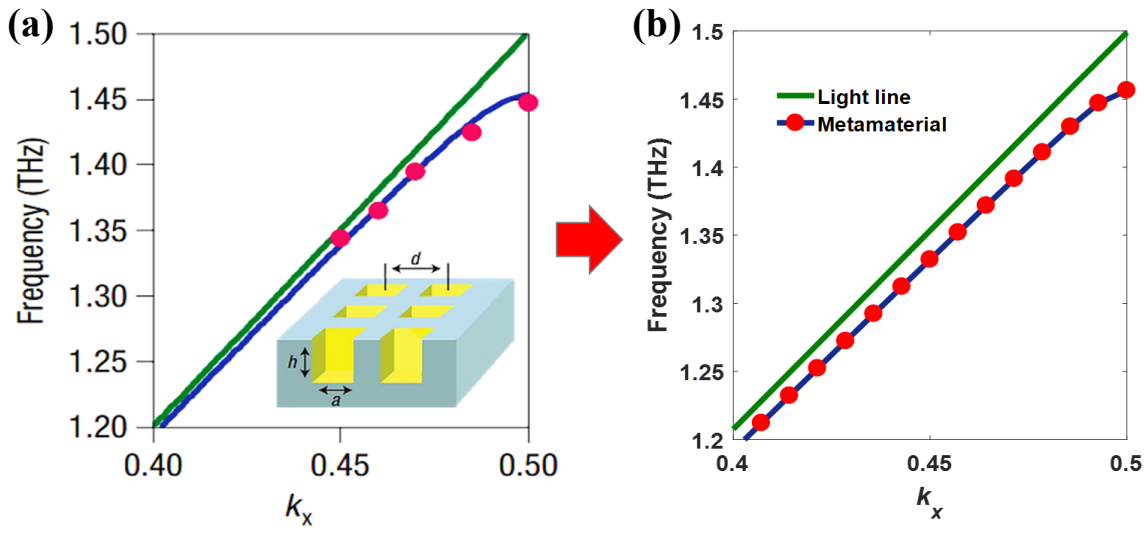

Fig. S10 (a) Dispersion relation (angular frequency ω versus propagation constant k_x) for plasmonic metamaterial accessed from Nature Photonics publication.[20] The green curve shows the light line, the blue curve shows the quasi-analytical modal expansion approximation (MEA) calculation, and red points indicate the FDTD simulation. The inset displays a schematic of the plasmonic metamaterial arrays of copper-lined holes. The geometrical parameters of the unit cell are *a*=66 µm, *h*=58 µm, and *d*=100 µm. (b) A resimulation of the dispersion relation results of the Nature Photonics publication[20] shows the great agreement of our simulation with the results of this article. (a) Reprinted with permission from Reference 20. Copyright 2008 Nature Publishing Group.

Table S3 Structural factors and performance of the proposed nanostructure absorber with those of similar recent works.

Material	Structure type	Lithography -free status	Thickness (nm)	Absorption Range > 90% (nm)	Peak Absorption (%)	Sim./Expt.	Reference
$TiN/MoS_2/SiO_2$ /Al	Nanodisk arrays	No	150	400–900	99% @500 nm & 680 nm	Sim.	[21] Huo et al., Nanoscale Research Letters 2017
TiO_2/TiN	Disks arrays	No	250	316–1426	99% @~1240 nm	Sim.	[22] Liu et al., Solar Energy Materials and Solar Cell 2017
TiO_2/Ti	Nanotube arrays	Yes	>2700	–	75% @300nm & 800 nm	Sim./Expt.	[23] Low et al., ACS Sustainable Chem. Eng. 2018
TiN	Nanodisk arrays	No	160	400–780	95% @700nm	Sim./Expt.	[24] Yu, et al., ACS Photonics 2021
TiN	Nanocavity (nanotube) arrays	Yes	250	200–800	99% @500nm	Sim./Expt.	[25] Mascaretti, et al., Nano Energy 2021
TiN	Nanohole arrays	No	200	~400–700	90% @500 nm	Sim./Expt.	[26] Mishra et al., J. Phys. Chem. C 2021
$Pt/TiO_2/Au$	Nanohole arrays	Yes	75	400–450	90% @400 nm	Sim./Expt.	[14] Jia, et al., ACS Photonics 2022
$TiO_2/SiN/SiO_2$	Pillar-arrays	No	230	–	85% @~350 nm	Sim./Expt.	[27] El-Jallal, et al., Optics Express 2022
TiN/GaN	Elliptical nanoantenna arrays	No	260	300–1116	99% @368 nm & 560 nm	Sim.	[28] Ashrafi, et al., Nanoscale 2024
TiO_2/TiN	**nanocavity (nanotube) arrays**	**Yes**	**330**	**200–1300 (in air) 200–1700 (in water)**	**99% @600 nm & 1020 nm**	**Sim.**	**Proposed nanostructure**

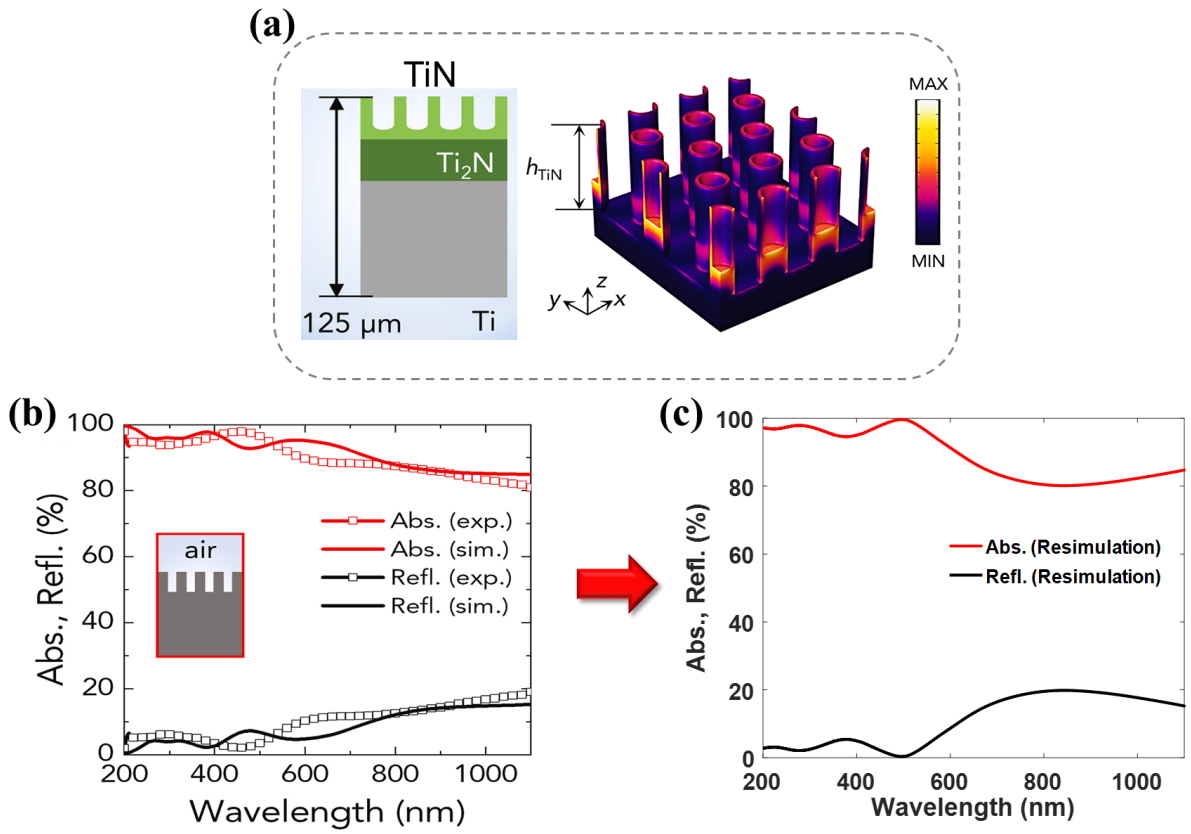

Fig. S11 Validation against available experimental data from the literature. (a) Schematic structure of the TiN-based solar absorber in Mascaretti's article:[25] TiN nanocavities (250 nm thickness), Ti_2N thermal layer (~ 1 μm), and the rest of the Ti substrate, as well as simulated power absorption across the nanocavities array. (b) Experimental (symbols) and simulated (solid lines) absorption (red) and reflectance (black) of the TiN-based solar absorber in air for Mascaretti's article.[25] (c) A resimulation of the results of the absorption spectra of the structure proposed in Mascaretti's article displays a good agreement of our simulation with the results of this article. The slight difference in our simulation compared with the results of the article can be due to the difference in the permittivity of the TiN material used in the simulations. (a, b) Reprinted with permission from Reference 25. Copyright 2021 Elsevier.

Table S4 Detail of PSO-ANFIS model.

Parameter	Value
Maximum iterations number	200
Maximum particles number	1000
Initial inertia weight (W_{min})	0.7
Inertia Weight Damping Ratio (W_{damp})	0.89
Cognitive acceleration (C1)	1
Social acceleration (C2)	2

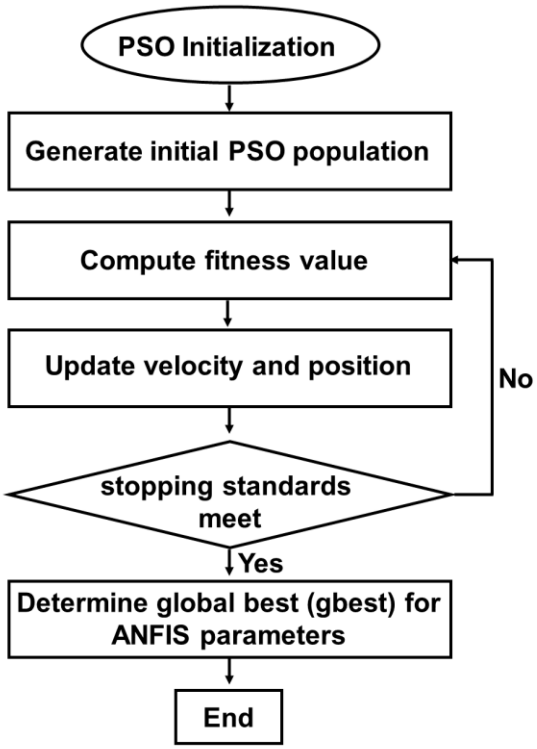

Fig. S12 Flowchart of the PSO-ANFIS model used in this study.

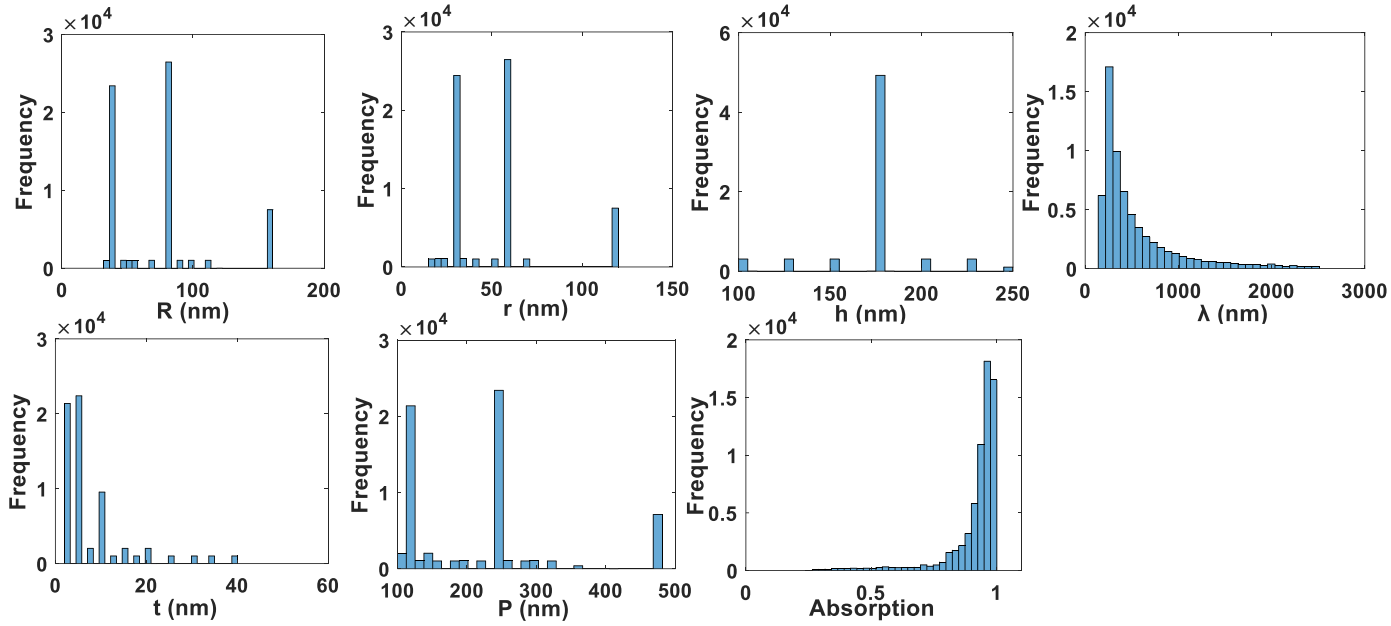

Fig. S13 Histogram of the data used in this study for the frequency and data distribution.

Table S5 Descriptive statistics of the data used in this study.

	Mean	STD	Min	Max	25%	Median	75%
R	73.5564	36.8918	35.0000	160.0000	40.0000	80.0000	80.0000
r	53.1285	28.1996	15.0000	120.0000	30.0000	60.0000	60.0000
t	7.7865	7.7742	2.5000	40.0000	2.5000	5.0000	10.0000
p	218.8010	109.5648	100.0000	480.0000	120.0000	240.0000	240.0000
h	172.6700	25.2059	100.0000	250.0000	175.0000	175.0000	175.0000
λ	551.9075	447.3292	200.0000	2500.0000	260.3624	372.5924	651.9345
Absorption	0.9177	0.1123	0.2467	1.0000	0.9113	0.9541	0.9768

References:

1 B. Doiron, M. Mota, M. P. Wells, R. Bower, A. Mihai, Y. Li, L. F. Cohen, N. M. Alford, P. K. Petrov and R. F. Oulton, *ACS Photonics*, 2019, **6**, 240-259.
2 K. Song, H. Lee, M. Lee and J. Y. Park, *ACS Energy Letters*, 2021, **6**, 1333-1339.
3 P. M. Voroshilov, V. Ovchinnikov, A. Papadimitratos, A. A. Zakhidov and C. R. Simovski, *ACS Photonics*, 2018, **5**, 1767-1772.
4 L. J. Mendoza-Herrera, M. C. Tebaldi, L. B. Scaffardi and D. C. Schinca, *Physical Chemistry Chemical Physics*, 2022, **24**, 28019-28028.
5 S. Ishii, S. L. Shinde, W. Jevasuwan, N. Fukata and T. Nagao, *ACS Photonics*, 2016, **3**, 1552-1557.
6 C. Tiburski and C. Langhammer, *ACS Photonics*, 2022, **10**, 253-264.
7 A. Naldoni, Z. A. Kudyshev, L. Mascaretti, S. P. Sarmah, S. Rej, J. P. Froning, O. Tomanec, J. E. Yoo, D. Wang and S. Kment, *Nano Letters*, 2020, **20**, 3663-3672.
8 S. Ayachi, X. He and H. J. Yoon, *Advanced Energy Materials*, 2023, 2300937.
9 C.-C. Chang, W. J. Kort-Kamp, J. Nogan, T. S. Luk, A. K. Azad, A. J. Taylor, D. A. Dalvit, M. Sykora and H.-T. Chen, *Nano Letters*, 2018, **18**, 7665-7673.
10 U. Mahajan, M. Dhonde, K. Sahu, P. Ghosh and P. M. Shirage, *Materials Advances*, 2024.
11 R. Mishra, A. Dubey, C.-W. Chang, A. Ranjan, M.-Y. Lu, T.-J. Yen and S. Gwo, *ACS Photonics*, 2022, **9**, 1895-1901.
12 A. Naldoni, U. Guler, Z. Wang, M. Marelli, F. Malara, X. Meng, L. V. Besteiro, A. O. Govorov, A. V. Kildishev and A. Boltasseva, *Advanced Optical Materials*, 2017, **5**, 1601031.
13 D. R. Lide, *CRC handbook of chemistry and physics*, CRC press, 2004.
14 H. Jia, Z. Li, B. Wang, G. Xing, Y. L. Wong, H. Ren, M. Li, K.-Y. Wong, D. Lei and L.-W. Wong, *ACS Photonics*, 2022, **9**, 652-663.
15 R. Katal, S. Masudy-Panah, M. Tanhaei, M. H. D. A. Farahani and H. Jiangyong, *Chemical Engineering Journal*, 2020, **384**, 123384.
16 C.-T. Li, S.-R. Li, L.-Y. Chang, C.-P. Lee, P.-Y. Chen, S.-S. Sun, J.-J. Lin, R. Vittal and K.-C. Ho, *Journal of Materials Chemistry A*, 2015, **3**, 4695-4705.
17 E. Rahman, J. Shin, S. Hong, S. Im, J. Kim, C. M. Chung, S. W. Hong, M. R. Hoffmann and K. Cho, *ACS Catalysis*, 2024, **14**, 8427-8436.
18 Y. Du, P. Liu, H. Zhang, L. Zou, K. Deng, X. Li, W. Tian and J. Ji, *Advanced Functional Materials*, 2024, **34**, 2309830.
19 C. Park, S. Ju, W. Kim, H. Sung, H. Song, J. Park, D. Chae and H. Lee, *Applied Materials Today*, 2024, **36**, 102063.
20 C. R. Williams, S. R. Andrews, S. Maier, A. Fernández-Domínguez, L. Martín-Moreno and F. García-Vidal, *Nature Photonics*, 2008, **2**, 175-179.
21 D. Huo, J. Zhang, H. Wang, X. Ren, C. Wang, H. Su and H. Zhao, *Nanoscale Research Letters*, 2017, **12**, 1-8.
22 Z. Liu, G. Liu, Z. Huang, X. Liu and G. Fu, *Solar Energy Materials and Solar Cells*, 2018, **179**, 346-352.
23 J. Low, L. Zhang, B. Zhu, Z. Liu and J. Yu, *ACS Sustainable Chemistry & Engineering*, 2018, **6**, 15653-15661.

24 M.-J. Yu, C.-L. Chang, H.-Y. Lan, Z.-Y. Chiao, Y.-C. Chen, H. W. Howard Lee, Y.-C. Chang, S.-W. Chang, T. Tanaka and V. Tung, *ACS Photonics*, 2021, **8**, 3125-3132.
25 L. Mascaretti, A. Schirato, R. Zbořil, Š. Kment, P. Schmuki, A. Alabastri and A. Naldoni, *Nano Energy*, 2021, **83**, 105828.
26 R. Mishra, C.-W. Chang, A. Dubey, Z.-Y. Chiao, T.-J. Yen, H. W. Howard Lee, Y.-J. Lu and S. Gwo, *The Journal of Physical Chemistry C*, 2021, **125**, 13658-13665.
27 S. El-Jallal, M. Hochedel, J. Capitolis, H.-S. Nguyen, C. Chevalier, J.-L. Leclercq, M. Amara, C. Seassal and E. Drouard, *Optics Express*, 2022, **30**, 29694-29707.
28 Z. Ashrafi-Peyman, A. Jafargholi and A. Z. Moshfegh, *Nanoscale*, 2024, **16**, 3591-3605.